PERGAMON

Journal of Structural Geology 25 (2003) 1675–1689

JOURNAL OF STRUCTURAL GEOLOGY

www.elsevier.com/locate/jsg

Faults and their associated host rock deformation: Part I. Structure of small faults in a quartz–syenite body, southern Israel

Oded Katz[a,b,*], Ze'ev Reches[a], Gidon Baer[b]

[a]*Institute of Earth Sciences, Hebrew University, Jerusalem 91904, Israel*
[b]*Geological Survey of Israel, 30 Malkhe Israel St., Jerusalem 95501, Israel*

Received 1 September 2001; received in revised form 1 August 2002; accepted 9 August 2002

Abstract

We analyze pervasive and discontinuous deformation associated with small faults in a quartz–syenite body in southern Israel. The analysis includes detailed mapping, measurement of in-situ mechanical rock properties and microstructural study of the faults. The mapped faults have 1–100-m-long horizontal traces, consisting of linked, curved segments; the segmented nature of the faults is also apparent at the 1–10 mm scale. The observed deformation features are breccia, as well as intra- and inter-granular fractures; these features are accompanied by reduction of the Young modulus and uniaxial strength of the host rock. The deformation features are zoned from a central fault-core through a damage-zone to the protolith at distances of 0.05–0.06 the fault length. Shear strains up to 300% were calculated from measured marker lines displacements and distortion in proximity to the faults. We argue here that the fault-related deformation during fault propagation is manifested by highly localized deformation in a process zone having a width of 0.001–0.005 of the fault length (fault-related deformation due to subsequent slip along the existing faults is analyzed in Part II). The observed self-similarity of the discontinuities over five length orders of magnitude and the outstanding lack of tensile microcracks suggest fault initiation and growth as primary shear fractures.

Keywords: Faulting; Mechanics; Deformation; Damage; Process zone

---

1. Introduction

Faulting of a rock body is always associated with deformation of the host rock. This deformation evolves in time and is generally distributed in distinct zones along and across the fault. The present study systematically documents fault-related deformation in proximity to small faults within a quartz–syenite intrusion and resolves the time evolution of this deformation. The host rock may be deformed during different stages of faulting: prior to faulting, during fault growth, and/or during the slip along an existing fault. Pre-faulting deformation is likely to be quasi-uniformly distributed in the faulted region and to reflect the stress/strain fields, that eventually lead to faulting (Aydin and Johnson, 1978; Lyakhovsky et al., 1997). Deformation during fault growth is probably concentrated at the fault-tip region (Chinnery, 1966; Cowie and Scholz, 1992; Anders and Wiltschko, 1994; Vermilye and Scholz, 1998), and reflects the concentrated local stress field that exists near the fault-tip zone (Pollard and Segall, 1987; Reches and Lockner, 1994). Further, deformation associated with slip along existing faults can be attributed to stress concentrations developed at irregular features along the faults such as steps between segments. Slip along irregular faults may generate pull-apart basins (Freund, 1974), or fault-bend-folds (Suppe, 1985). Fault related deformation may be manifested by microdamage over a large region (Lyakhovsky et al., 1997), small microcracks localized at the fault tip region (Vermilye and Scholz, 1998), gouge zones of crushed host rocks at the fault core (Chester and Logan, 1986), jointing, secondary faults such as Riedel shear developed in a wide zone (Aydin and Johnson, 1978), population of fractures developed locally at fault tips (Chinnery, 1966), and fold-like linking between segments (Sylvester, 1988).

Some patterns of fault-related deformation may be attributed to a specific model of faulting, and several such models are outlined here. (1) Griffith (1924) proposed that a

---

[*] Corresponding author. Correspondence address: Institute of Earth Sciences, Hebrew University, Jerusalem 91904, Israel. Fax: +972-2-5380688.

E-mail address: odedk@mail.gsi.gov.il (O. Katz).

0191-8141/03/$ - see front matter © 2003 Elsevier Science Ltd. All rights reserved.
doi:10.1016/S0191-8141(03)00011-7

fault nucleates at a critical flaw and it is expected to grow within its own plane; hence pre-faulting deformation is not predicted by Griffith's model. Micromechanical observations, however, have showed that rocks contain many tensile microcracks that are active before and during faulting (Tapponnier and Brace, 1976; Krantz, 1979). Hence it is generally accepted that growth and interaction of tensile microcracks, not necessarily parallel to the shear plane, control macroscopic faulting. (2) A few analyses proposed that a fault grows in the wake of a process zone, a finite size region of high stress concentration at the fault tip in which the intact rock is disintegrated (Cowie and Scholz, 1992; Reches and Lockner, 1994). These models predict that fault related damage is concentrated close to the fault and decays away from it. (3) Damage models are based on the assumption that a fault forms due to interaction among many damage points, mostly microcracks. These microcracks that were generated prior to faulting are assumed to coalesce when their density reaches a critical value (Peng and Johnson, 1972; Horii and Nemat-Nasser, 1985; Ashby and Sammis, 1990; Moore and Lockner, 1995; Lyakhovsky et al., 1997). These models predict that microcracks are not necessarily restricted to the fault tip, and that the density of microcracks away from the fault is comparable with the density of microcracks along the initial fault.

The central objective of the present work is to document the deformation associated with natural small faults. We divide the fault region into three zones (Fig. 1) following Caine et al. (1996): (1) the 'fault-core', a narrow zone of highly disintegrated rock that accommodates a large amount of localized shear; (2) the 'damage-zone', a wider zone of gradually decreasing intensity of the fault related deformation; and (3) the 'protolith' a region with negligible fault-related deformation. Using this framework, we analyze the in-situ deformation associated with three small faults in a quartz–syenite body in southern Israel (Fig. 2). The analyzed discontinuities, which range in length over five orders of magnitude, reveal deformation structures that are distributed along the faults within zones of characteristic width similarly to Fig. 1. We discuss here the timing and evolution of the observed fault related deformation. The mechanics of fault nucleation and growth will be presented by Katz et al. (in preparation).

2. Field analysis of the faults and their associated deformation

2.1. General setting

We analyzed small faults within a shallow intrusion in Gevanim dome, Ramon area, southern Israel (Baer and Reches, 1989) (Fig. 2). This quartz–syenite body intruded the calcsilicate–carbonate sequence of Triassic age about 130 Ma ago (K–Ar whole rock dating by Lang and Steinitz (1989)). Several faults divide the intrusion into a few blocks that cover an area of ~1 km^2; the intrusion thickness is at least 100 m. Gevanim quartz–syenite is composed of 5–20% quartz, about 5% sanidine and 70–80% albite and small amounts of melanocratic phases. Alteration of feldspar to secondary calcite and cavity-filling calcite is common. The studied area is located in the central part of the largest block in the intrusion (Fig. 2), about 20–30 m below the roof of the intrusion and at least 50 m away from its lateral margins. The grain size of the rocks in the studied area is 0.19 ± 0.03 mm and it decreases towards the intrusion margins.

The quartz–syenite intrusion of Gevanim dome is crosscut by many discontinuities, including several sets of faults, joints, veins and breccia zones. In the present work we used the word 'fractures' for discontinuities that have no clear sense of motion, 'faults' to indicate shear fractures (mode II/III), and 'joints' to indicate dilational fractures (mode I). The most dominant fracture set trends in an N–S direction and it was mapped at 1:500 scale with a total station (EDM) (Fig. 3); the two other fracture sets strike E–W and NW–SE. The general nature of these sets is described below.

The N–S set is composed of vertical fractures with strike that ranges from NNW to NNE (Fig. 3). They are spaced up to 1 m apart and some of them are tens of meters long (Fig. 3a). Some field observations indicate that the fractures of the N–S set are right-lateral, strike-slip faults: (1) many of them display systematic right-lateral separation of traces of the older E–W fractures (Figs. 4–6); (2) some of them carry horizontal slickenside striations; (3) the deformation style at the links between segments is compatible with right-lateral slip component (see below); and (4) no evidence was found for dilation across the faults or for dip-slip components. Thus, we regard the N–S fractures as right-lateral, strike-

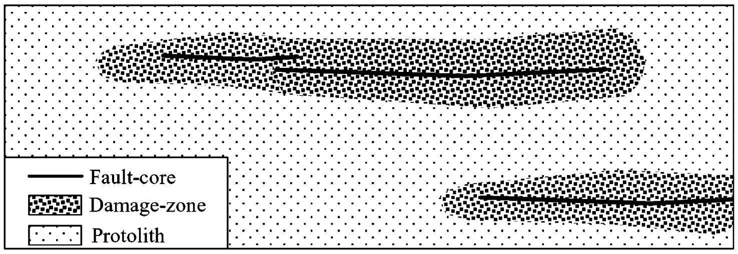

Fig. 1. Schematic zonation of fault-related deformation along a fault (after Caine et al., 1996).

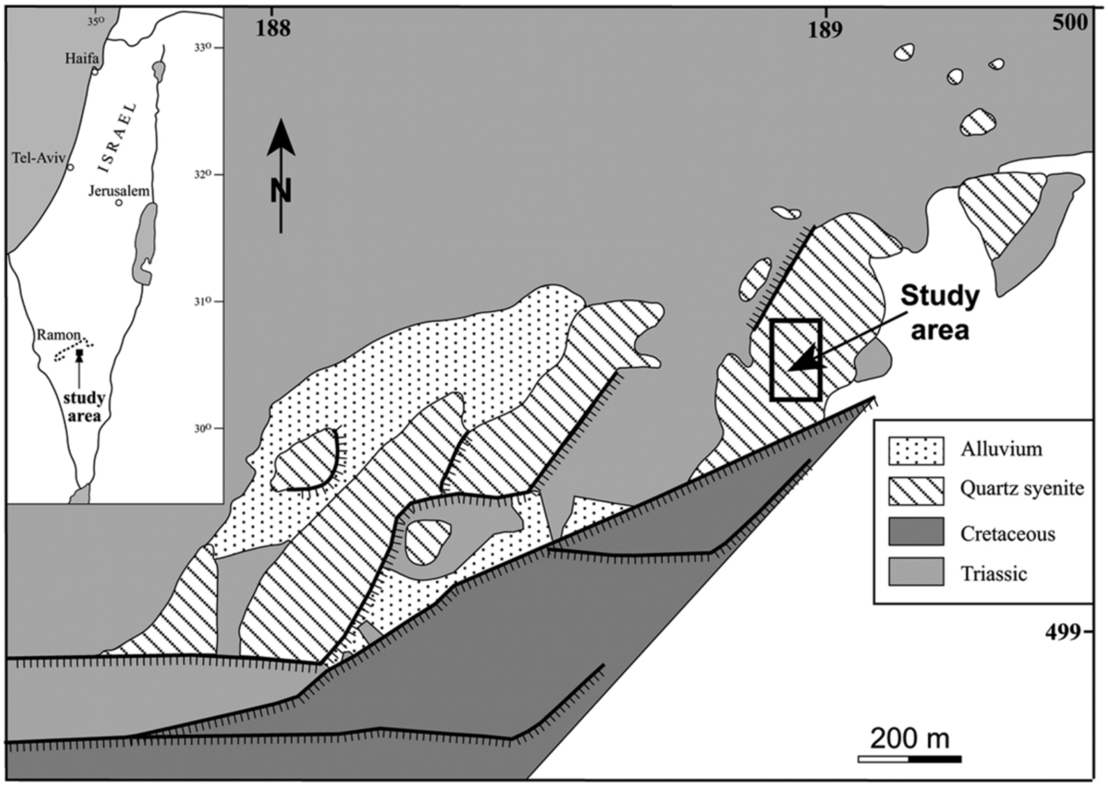

Fig. 2. Simplified geological map of Gevanim Dome, Ramon area, southern Israel (after Zak, 1960); inset is location of Gevanim Dome. Study area (marked by the rectangular frame) is about 20–30 m below the roof of the intrusion and at least 50 m away from its lateral margins.

slip faults. Sense and amount of slip on a given fault segment were ascertained only when three or more traces of the E–W fractures are similarly displaced. The amount of right-lateral slip on a fault segment varies with the strike of this segment (Fig. 3b): slip along NNE striking fault segment is zero to a few centimeters, slip along N-striking fault segments is up to a few tens of centimeters, whereas slip along a single NNW-striking fault segment exceeds 125 cm (Fig. 3). Faults in the NNE direction have narrow fault-zones of a few millimeters width, and they have relatively smooth traces with minor segmentation. Faults in the NNW direction have wider fault zones, up to 15 cm wide, and display crooked traces with intense segmentation. From this spatial arrangement with finite slip increasing in faults that have a more westerly strike, it is deduced that this set of strike slip faults developed under maximal horizontal compressive stress trending approximately NE–SW (Fig. 3c).

The fractures of the E–W set are sub-vertical joints and veins filled with polymetallic sulfo-arsenitic mineralization (Itamar and Baer, 1993). The filling is a few millimeters to a few centimeters wide with local occurrence of host rock fragments. The E–W fractures commonly form swarms of several, sub-parallel, curved tensile fractures. The mineralization filling the E–W set is 125 ± 2 Ma old suggesting that these fractures formed in a chilled brittle external part of the intrusion during emplacement (Itamar and Steinitz, 1988). The third, least dominant set of SE–NW-trending fractures comprises sub-vertical, relatively short, discontinuous joints. Usually these fractures are not dilated and they appear to terminate toward the fractures of either E–W or N–S sets. These field relations suggest that the SE–NW set is younger than the E–W set, and penecontemporaneous to (or younger than) the N–S set of faults.

The study now focuses on detailed analysis of three faults selected from the N–S fault set. We found that these three faults represent different stages of fault evolution as manifested by their length, width of the fault-zone, amount of slip and segmentation, as well as host rock deformation and microstructure.

2.2. Fault geometry of three right-lateral faults

The three selected faults of the N–S set are marked GF1, GF2 and GF3. The exposed trace of GF1 is 15.5 m long and its central portion ~5 m long was mapped at scale of 1:10 (Fig. 4a). The map displays four segments with lengths of 0.8–2.0 m, and a general trend of 0–015° with local deviations up to 30° (Fig. 4a). The northern portion consists of two parallel segments, 7 cm apart that bound a partially crushed block. The systematic slip distribution along GF1 displays two local maxima of 29 and 40 mm at distances of 5 and 12 m south of its northern tip (Fig. 4b). This slip distribution suggests that GF1 is composed of two, linked segments that are ~8 m (southern segment) and ~4 m (northern segment) long; the link between these segments (marked II in Fig. 4a) shows that they are currently

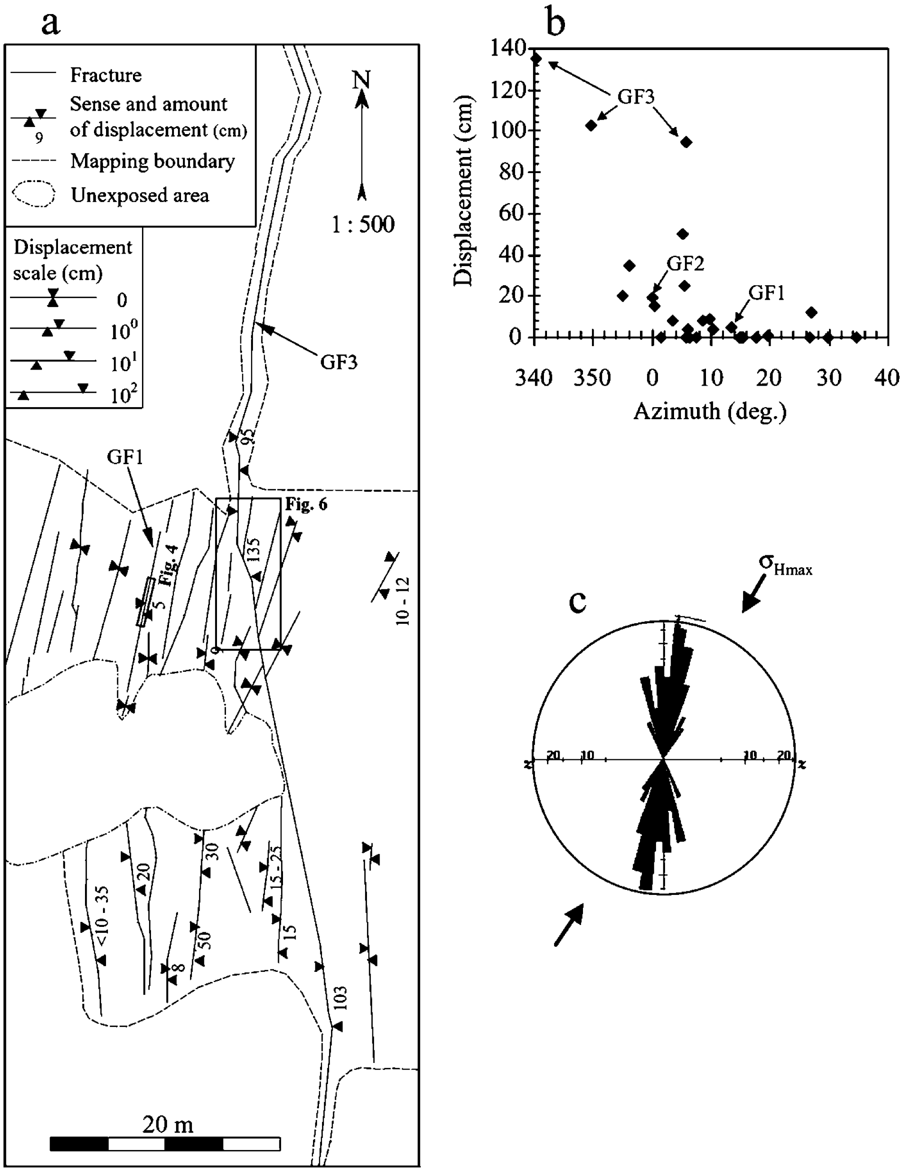

Fig. 3. The N–S fault set in Gevanim qz–syenite. (a) Fracture map showing dominant N–S faults, as mapped at scale of 1:500 by EDM Total Station teodolite; right-lateral displacements are marked. Areas of detailed mapping on GF1 and on GF3 (Figs. 4 and 6, respectively) are marked. GF2 is located about 50 m west of the mapped area. (b) Individual fault segment displacements versus the segment strike. (c) Length-azimuth, area weighted rose diagram plot showing distribution of all faults in (a) (total cumulative length is 400 m; $n = 27$); deduced σ_{HMAX} direction, the axis of maximal horizontal compressive stress (see text).

continuous with one another. The fault-core of GF1 is narrow, about 1 mm wide in the north and about 10 mm wide and calcite-filled in the south. Breccia was not observed along GF1.

GF2 is located about 50 m west of the area mapped in Fig. 3. Its trace is about 7.5 m long with a clear northern tip and a poorly exposed southern one (Fig. 5a and b). GF2 displays four segments with lengths of 1.2–2.6 m and local trends from 350° to 010° (Fig. 5a). Right-lateral slip along GF2 increases from zero at the north tip to an approximately constant value of 19.0 ± 3.0 mm along the rest of the fault (Fig. 5c). The northern end displays abrupt reduction of the slip (Fig. 5c), and bending of the fault trace towards 030° (Fig. 5a). This bending of GF2 is compatible with fault splays into the dilational quadrant of a right-lateral fault (Segall and Pollard, 1980). A few fractures with minor dilation and up to 5 mm slip appear in an en-échelon pattern at a distance of 1 m north of the fault (Fig. 5a). Bands of crushed rock that strike 030° also appear in this area (Fig. 5a); their structural relations to GF2 are not clear. The fault-core of GF2 is 1–20 mm in width, and it contains brecciated, crushed host rock (see Microstructure below). The steps between the segments with left offset generate small, up to 20 mm wide, breccia regions (Fig. 5a).

The longest mapped fault is GF3 with an exposed trace of 100 m (probably longer) and general trend of NNW (Fig. 3). GF3 consists of at least 10 segments with lengths of 2–38 m, local trends of NNE (015°) to NNW (340°), and slip

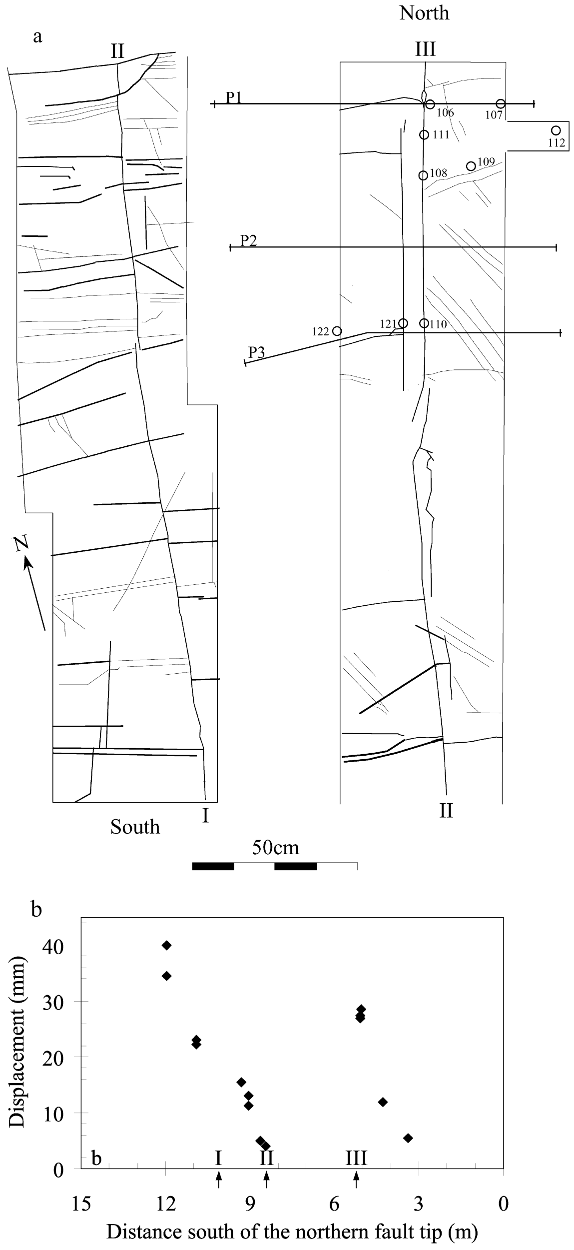

Fig. 4. Central portion of Gevanim Fault 1 (GF1) (for location see Fig. 3). (a) Map, 1:10 mapping scale, displaying fault trace, E–W fractures, sample locations (106–112, 121 and 122) and hammer profiles (legend in Fig. 5); Roman numbers I–III mark connection points of stretches. (b) Displacements along GF1 from offset E–W fractures plotted with respect to distance from northern fault tip; Roman numbers indicate locations shown in (a).

magnitude of 25–125 cm. A 5-m-long stretch of GF3 was mapped at 1:10 scale (Fig. 6); its well-exposed NNW-trending segments have the largest observed slip in the entire studied area. The fault has a left-stepping zone with ~0.5 m offset between en-échelon NNW and N–S segments. In the mapped stretch, the fault-core consists of two major breccia zones that are up to 15 cm wide and a few additional narrow breccia zones. The breccia zones consist of pebble-sized fragments cemented by calcite and the host rock adjacent to the breccia zones is apparently intact. The cumulative slip along GF3 is 125 cm (d–d″; Fig. 6), 65 cm on the western segment (group d–d′; Fig. 6), 45 cm on the eastern segments (d′–d″), and 15 cm on minor segments inside the central block.

2.3. Distributed damage within the host rock

We used a Schmidt hammer (model 58-C181/F by Controls) to evaluate the in-situ mechanical properties of the host rock in proximity to the selected faults. The Schmidt hammer was originally developed for non-destructive testing of concrete strength. Katz et al. (2000), derived empirical correlations between the hammer rebound and the Young's modulus, uniaxial strength and bulk density of the tested rocks. They also described the procedures for in-situ, field measurements. In the current study, hammer measurements were conducted along seven profiles (Figs. 4a, 5a and 6), each with 8–17 measurement points, and each point was subjected to tens of hammer impacts (Fig. 7; Table 1). All points were on grinder polished surfaces except profile 4 with manually polished surfaces.

The hammer rebound (HR) values in four profiles (1, 2, 5 and 7 in Fig. 7) can be divided into two distinct groups, one of high values and a second of low values; for example, along profile 1, the group of high values is HR = 75 ± 1, versus the second group of HR = 49 ± 11. Two other profiles (4 and 6) also show two groups but with smaller differences in rebound values; for example, along profile 6, the high value group has HR = 71 ± 1 versus the second group of HR = 69 ± 0. Profile 3 has a constant value of about HR = 72 ± 1. To quantify the local variations of the rebound values, we convert the hammer readings to Young's modulus (E), compressive strength (U) and bulk density (D) using our calibration (Katz et al., 2000) (Table 1). We refer to these three parameters as indicating the in-situ 'competence' of the rock.

The competence variations revealed three noticeable features. First, high competence values are located away from the faults, whereas lower competence values appear at the fault-zones (Fig. 7; Table 1) (with local exception along profile 4). A comparison between the background competence (away from the fault) and the fault-zone competence is displayed in Fig. 8. The largest competence reduction appears across profiles 1 and 2 of GF1 with a decrease of more than 50% of E and U in the fault zone; the other profiles show a corresponding decrease of up to 30% of E and U. Second, the fault-normal width of the competence reduction zone is scattered (Fig. 7; Table 1), and it is weakly proportional to the fault length. For example, the width of this zone is ~7 cm for 15.5-m-long GF1 and more than 33 cm for the ~100-m-long GF3. Third, the background competence values at the proximity of GF3 are the lowest background values in the study area (Figs. 7 and 8; Table 1). This observation may indicate that the competence

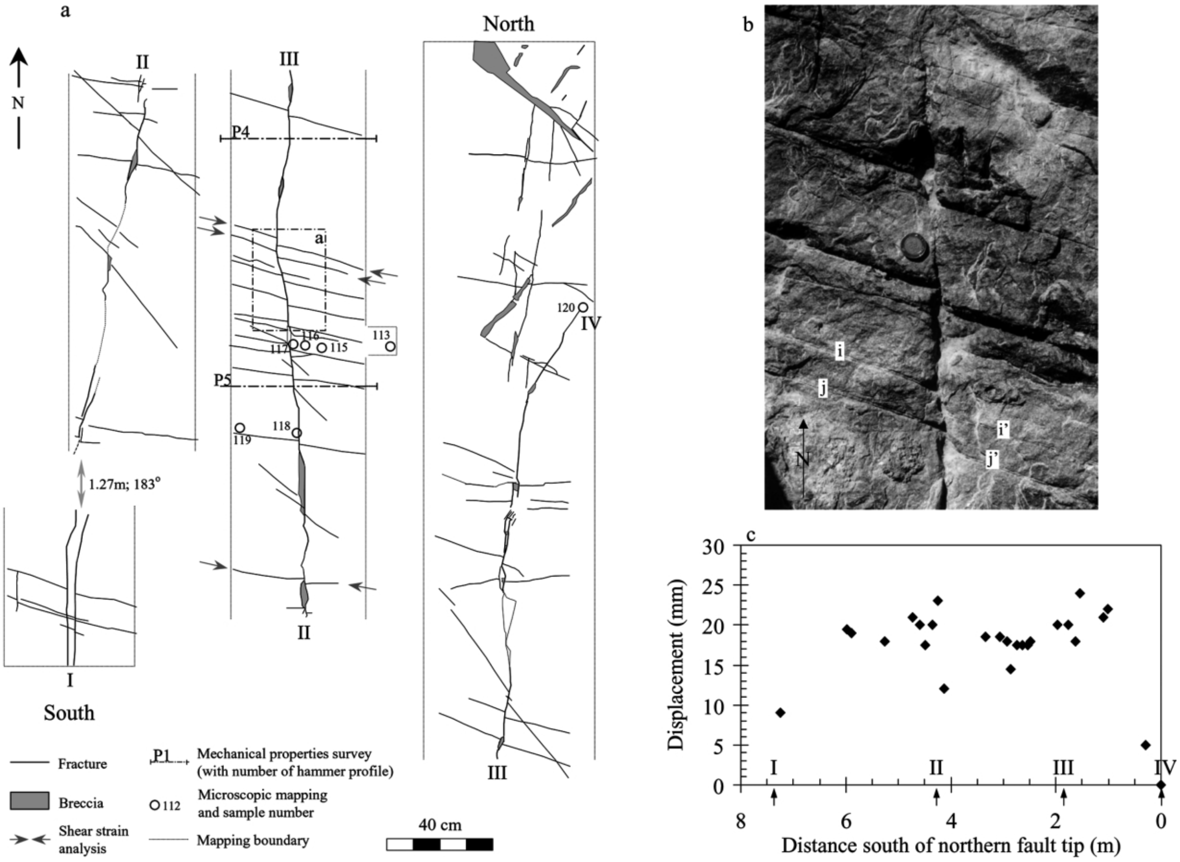

Fig. 5. Gevanim Fault 2 (GF2) (located 50 m west of the area mapped in Fig. 3). (a) Map, 1:10 mapping scale, displaying fault trace, E–W fractures, sample locations (113–119) and hammer profiles (see legend); Roman numbers I–III mark connection points of stretches. (b) Picture showing the central part of the fault; note displaced E–W fractures: i and j to i′ and j′, respectively. (c) Displacements along GF2 from offset E–W fractures; plotted with respect to distance from northern fault tip; Roman numbers indicate locations shown in (a).

Table 1

Summary of Schmidt hammer field survey of seven profiles (locations in Figs. 4–6). The results are presented by mean values of background readings from both sides of the fault and the mean values for the fault zone; *W*—fault normal distance of competence reduction (Fig. 7). The hammer rebound units (H.R.) were used to evaluated Young's modulus (*E*), compressive strength (*U*) and bulk density (*D*) according to Katz et al. (2000)

		W (cm)	H.R.	*E* (GPa)	*U* (MPa)	*D* (kg/m^3)
GF1						
Profile 1	Background average	10	75 ± 1	79 ± 4	329 ± 26	2768 ± 20
	Fault zone minimum		49 ± 11	21 ± 18	58 ± 62	2210 ± 262
Profile 2	Background average	7	72 ± 1	69 ± 4	268 ± 26	2712 ± 26
	Fault zone minimum		55 ± 6	31 ± 11	89 ± 42	2371 ± 132
Profile 3	Background average	0	72 ± 1	72 ± 4	284 ± 23	2729 ± 21
	Fault zone average		Reading as background			
GF2						
Profile 4	Background average	10	74 ± 1	76 ± 3	300 ± 25	2743 ± 22
	Fault zone average		72 ± 1	70 ± 2	274 ± 12	2720 ± 12
Profile 5	Background average	25	73 ± 1	73 ± 3	292 ± 16	2736 ± 15
	Fault zone average		69 ± 0	63 ± 1	230 ± 6	2672 ± 7
GF3						
Profile 6	Background average	21 <	71 ± 1	68 ± 2	259 ± 13	2704 ± 14
	Fault zone average		69 ± 0	62 ± 0	230 ± 0	2671 ± 0
Profile 7	E. background average	33 <	72 ± 0	70 ± 1	276 ± 7	2722 ± 7
	W. background average		69 ± 1	60 ± 2	219 ± 12	2657 ± 16
	Fault zone average		66 ± 1	55 ± 1	188 ± 7	2614 ± 11

W—Fault normal distance of competence reduction; H.R.—relative hammer rebound units; *E*—in-situ Young's modulus; *U*—in-situ compressive strength; *D*— in-situ bulk density.

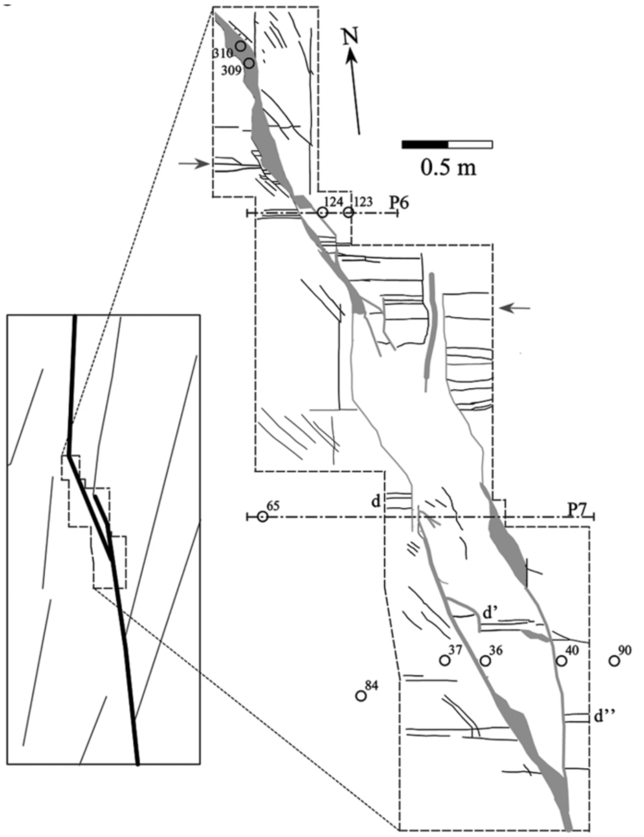

Fig. 6. Details of overlap zone between two segments of Gevanim Fault 3 (GF3) (for location see Fig. 3). The map, at 1:10 mapping scale shows the fault trace, E–W fractures, sample locations (36, 37, 40, 65, 84, 90, 123, 124, 309 and 310) and hammer profiles (legend in Fig. 5). Note offset of groups of E–W fractures, i.e. group d is displaced 0.65 m to d′ on the western segment and again 0.45 m to d″ on the eastern segment; additional displacement of 0.15 m is distributed between the two segments.

reduction zone associated with GF3 is wider than the length of the hammer profiles.

2.4. Distortion of lines at the faults' proximity

One striking field observation is the distortion of traces of some EW fractures in proximity to faults GF2 and GF3. We measured this distortion by first aligning a thin thread to the fracture trace on both sides of the fault (dashed line in Fig. 9), and then measuring the deviation of the trace from the thread as a function of distance from the fault ($v(x)$ in Fig. 9). The distorted traces are assumed to have been linear and continuous prior to faulting. We used this technique to measure three traces across GF2 (locations marked with gray arrows in Fig. 5a). For GF3, we used an EDM system (accuracy ± 3 cm) to measure a distorted swarm of fractures (location marked with gray arrows in Fig. 6). The results (Fig. 10) show that the line distorted is recognized to distances of 0.2–0.4 m away from GF2, and 4–6 m away from GF3. The structural significance of these measurements and their implications to fault evolution are analyzed in Part II (Katz and Reches, in review).

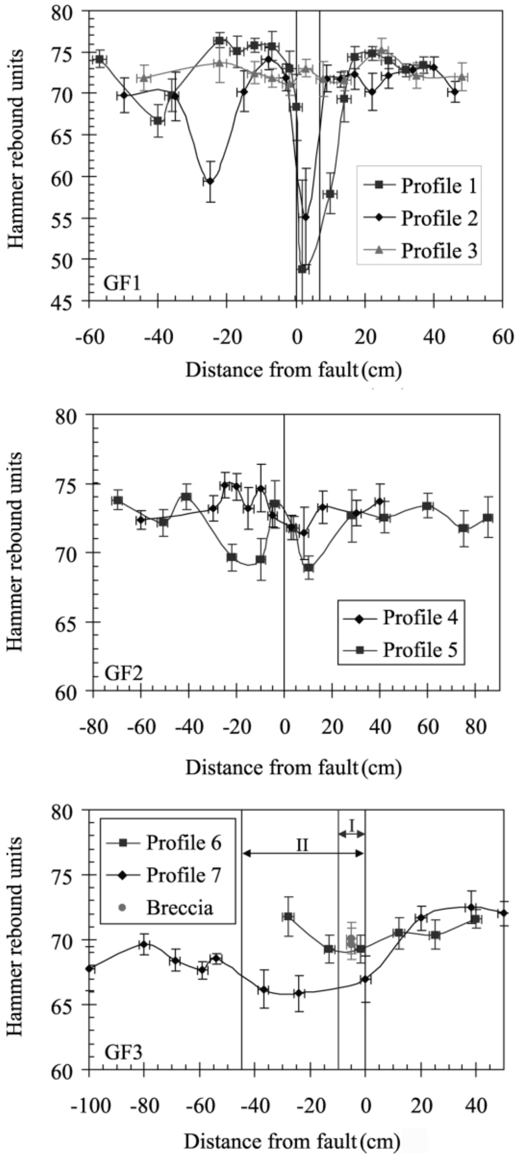

Fig. 7. Schmidt hammer field profiles showing hammer rebound units along the seven profiles; fault traces are marked by vertical thin lines; profile locations are shown as dashed–dotted lines in Figs. 4–6; field and analysis procedures are specified in the text and in Katz et al. (2000). The arrows marked I and II in the lower figure are the width of the fault trace at profiles 6 and 7, respectively.

3. Microstructural analysis

A total of 26 vertical cores of 25.4 mm diameter were collected from the vicinity of the selected faults (locations in Figs. 4–6; summary in Table 2); microstructural analysis was conducted on horizontal, oriented thin-sections prepared from these cores. The thin-sections were mapped at scale of 40:1 by using an optical microscope together with scanned computer images. In addition we used SEM images (produced on Jeol-JXA-8600) for 1000:1–200:1 scale examination of the microstructures.

We found four types of microstructures: fault-oblique microfractures, fault-parallel microfractures, calcite-filled-

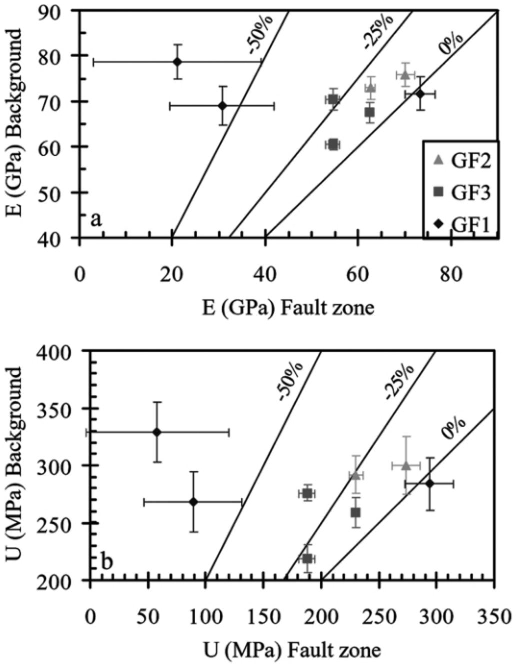

Fig. 8. Comparison of background versus fault-related competence parameters according to Schmidt hammer analysis along seven profiles (Fig. 7; Table 1). (a) Young's modulus, E; (b) Compressive strength, U. The diagonal lines show the marked percentage of competence reduction close to the fault.

networks and breccia zones; all will be described in detail below. The fault-oblique microfractures were found in all samples regardless of fault-distance, and are regarded by us as unrelated to the dominant N–S faulting. The three other types of microstructures display systematic distribution with respect to the damage zonation. We found no intragranular, tensile microfractures that can be related to the N–S faults; this remarkable lack of intragranular, tensile microcracks is in agreement with our triaxial experiments on Gevanim quartz–syenite samples (Katz and Reches, 2000). The implications of this observation will be analyzed in a following manuscript (Katz and Reches, in preparation).

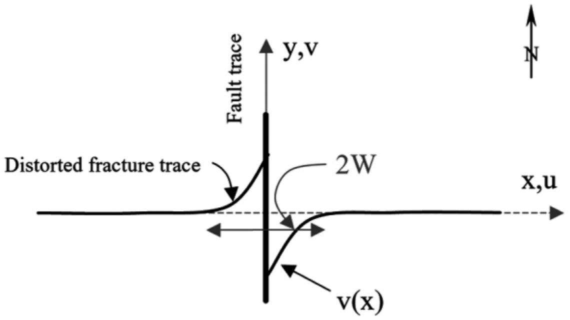

Fig. 9. Schematic presentation of the distortion of linear fracture traces in proximity to GF2 and GF3. Heavy N–S line—the fault; thick, curved lines—the E–W-trending fractures distorted near the faults; dashed E–W lines—linear fracture traces prior to faulting. The coordinate system of deformation analysis: x, y—fault normal and fault parallel axes; u, v—corresponding displacements; [$v(x)$]—a distorted line that was initially normal to the fault; $2W$—width of distortion zone.

The microstructures are described in detail below for the fault core and the damage-zone.

3.1. Fault-core

The microstructure of fault-cores was analyzed in thin sections made from 10 samples drilled into the cores of the three studied faults (Figs. 4–6; Table 2). In the field, GF1 displays a quasi-planar, thin zone of varying width (0.1–10 mm) and with no breccia. In thin-sections, the internal part of the core consists of opaque oxide (Fig. 11a–d), quartz cement of 10–50 μm grain-size (Fig. 11a and b) and brown, green or clear calcite that fills thin veins, which cut the oxide (II in Fig. 11d). Clear calcite cement also fills an irregular network of interconnected fractures and cavities (Fig. 11a–d). A few rock fragments appear along the core (α in Fig 11c and d).

In the field, the fault-core of GF2 is up to a few tens of millimeters wide with few bands of micro-breccia (fragments are up to 0.2 mm). In thin-sections, the fault-core of GF2 (Fig.12a and b) consists of several quasi-linear zones of micro-breccia that strike 345–015°. Each zone is 0.25–1.25 mm wide and contains angular rock fragments of the quartz–syenite (α in Fig. 12a and b) cemented by brown, greenish-brown (β in Fig. 12a and b) and clear calcite ($\beta 1$ in Fig. 12b). A few E–W-striking fractures are cut and displaced by the brecciated zones (IV in Fig. 12a and b).

In the field, the fault-core of GF3 is an about 100-mm-wide breccia. In thin-sections, the breccia is cemented by brown calcite, which includes a system of 0.5–1.5-mm-wide bands of poorly sorted angular fragments, 0.01–0.40 mm in size (gouge?) (α in Fig. 12c). Narrow zones of host rock fragments appear between these bands (γ in Fig. 12c). The fragments in the bands indicate a mixture of opening, shear and rotation modes. Fault parallel (NNW–NNE) breccia bands cemented by clear calcite locally cut the GF3 main breccia. This clear calcite breccia consists of angular rock fragments up to 1 mm in size.

In summary, the studied three faults are characterized by an abundance of cementation by secondary quartz and calcite in networks and veins, dominance of micro-breccia and negligible amount of gouge.

3.2. Damage-zone

Two types of microstructures dominate the damage-zone (Fig. 1): calcite-filled-networks and microfractures. A calcite-filled-network consists of inter-connected small cavities filled with light-yellow calcite locally rimmed with brown calcite. The cavities are less than 0.01 mm in size and they are associated with intragranular and short intergranular fractures. Most of the fractures in the calcite-filled-networks are aligned in a N–S direction (δ in Fig. 12a and b). Larger, filled voids (> 1 mm) may also be part of a calcite-filled-network (Fig. 11a and b).

Microfractures are by far the most dominant structures in

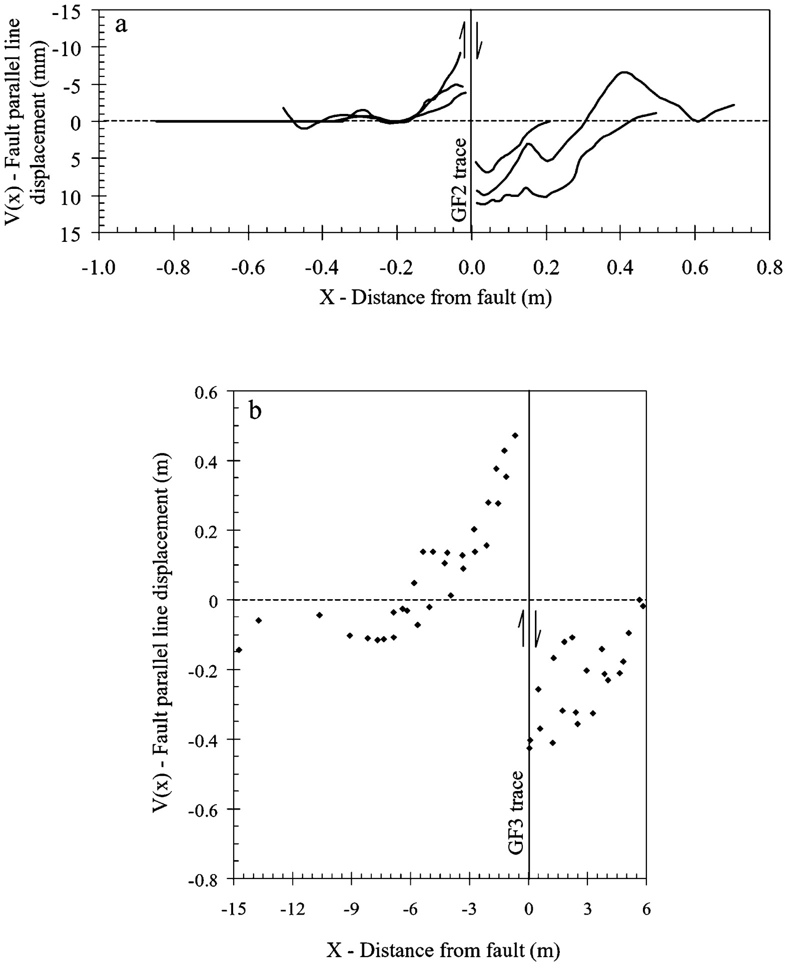

Fig. 10. Line distortion across GF2 and GF3; coordinates defined in Fig. 9, dashed horizontal line in the x coordinate is a reference line. (a) Three field-measured profiles of fracture traces across GF2 (locations in Fig. 5); shown fault-parallel line displacement, $v(x)$, with respect to initial position. (b) A distortion profile measured across GF3 (location in Fig. 6); diamonds are points measured on a E–W fracture swarm with EDM total-station. Vertical exaggeration of $v(x)$ is the same in (a) and (b).

the thin-sections. They display a wide range of properties: intergranular and transgranular, length range from <1 to >25 mm, width range of 0.01–1.0 mm, and orientations and crosscutting relations that vary considerably. Most of the microfractures are filled with secondary minerals (Fig. 13) and their composition was studied by the electron microprobe. We found clear calcite (massive or granular), dark brown calcite with iron oxides and greenish brown calcite with clays. Rock fragments within the fractures are enclosed in brown calcite (α in Fig. 13a). Less abundant fracture fillings are fine-grain quartz and opaque black or brown oxide. The amount of slip along the microfaults varies from 0.1 to 5 mm according to the displaced crystals (Fig. 14). The microfractures commonly display en-échelon patterns, including pull-apart openings (Fig. 14). Displacements are dextral in most cases (eight out of nine observed micro-faults) although sinistral displacements were also observed. The microfaults with evident shear displacement consist of rock fragments enclosed in brown calcite.

The microfractures can be divided on the basis of their direction into a fault-parallel group that strikes in the range of NNW to NNE (Fig. 15a) and a fault-oblique group that strikes mainly in the range NW to SW (Fig 15b and c). The few observed crosscutting relations indicate that the fault-parallel microfractures and microfaults cut and displace the fault-oblique microfractures; for example, truncation and apparent displacement at point IV in Fig. 12a and b. These relations suggest that the fault-parallel microfractures are younger.

The crosscutting relations of the fracture fillings indicate the following relative ages (from early to late): (a) opaque oxides (crosscut by fine-grain quartz, I in Fig. 11b; brown calcite, II in Fig. 11d; and clear calcite, III in Fig. 11b and d); (b) fine-grain quartz (crosscut by brown calcite, IIa in Fig. 13b; and clear calcite, III in Fig. 11b and IIIa in Fig. 13b); (c) brown (and greenish brown) calcite (crosscut by clear calcite, IIIb in Fig. 11d and IIIb in Fig. 13b); (d) clear calcite (Figs. 11a–d and 13a and b). The opaque oxides belong to the crystallization phase of the quartz–syenite intrusion (Early Cretaceous; Itamar and Steinitz, 1988). The age of the fine-grain quartz is unknown. The (c) and (d) fillings appear between angular rock fragments and veins (α

Table 2

Summary of microstructural analysis of 26 thin-sections from samples collected across the three studied faults in Gevanim. Sample locations are shown in Figs. 4–6. Samples 108, 110, 121, 117 and 118 include the fault core and additional area of about 1 cm at its proximity

	Sample (#)	Distance from fault core (cm)	Microstructures		
			Fracture direction	Fracture fill[a]	Other[b]
GF1	108, 110, 121	0, 0, 0	N (360–015°)	OX, FQ, BC, PC	CC, IC
			N	BC	
			NW	OX, FQ, BC, PC	
			NE	BC(+RF), PC	CC, IC
	106, 111	2, 2	W	OX, FQ	
			NE	OX, PC	
	109	9	N	PC	
			N–NE	BC, PC	
			W	BC(+RF), PC	
	122	15	WSW	FQ	
	107, 112	30, 35	NNW	BC, PC	
			NE	BC	
GF2	117, 118	0, 0	N (345–015°)	GC, BC, PC, RF	CC
	116	4	N, NNE[c]	BC(+RF), PC	IC, CC
			W	BC(+RF), PC	IC, CC
			NW	PC	
			Intergranular	PC	Rare
	120	2 N of the tip	NNW[c]–NNE	BC(+RF), PC, FQ	
			E–NE[c]	BC(+RF), PC	CC
			WNW	FQ	
	115	11	NW[c]	BC(+RF), PC	
			NE	BC(+RF), PC	
			N	PC	
	113,119	45, 23	NW	BC(+RF), PC	
			NE	BC, PC	
GF3	309, 310	Breccia zone	No directional data	BC(+RF)	IC
	36, 40	4, 4	NNE	BC(+RF), PC	CC, IC
			W–N	BC(+RF)	CC, IC
	124	4	non (breccia)	BC(+RF)	CC, IC
			NNW–NNE	PC(+RF)	
			W	BC(+RF), PC	
	123	13	NNW[c]–N[c]	BC(+RF), PC	IC
			NE–E	OX, PC	
	37, 90	18, 28	NW[c]–N	BC(+RF), PC	CC, IC
			NE	BC(+RF), PC	
	84	72	NNE	PC, BC	CC, IC
			W	PC	
	65	85	N[c]	PC, BC	IC
			NW	BC, PC	

[a] B/G/PC—brown/green/clear calcite; FQ—fine grain quartz; RF—rock fragments; OX—Opaque oxides.

[b] I/CC—intergranular/cavity fill calcite in the fractures and the host rock.

[c] Evidence for shear displacement on fractures of this direction.

in Figs. 12 and 13) that are related to slip and dilation along the fractures.

4. Zonation of fault-related deformation

Our field and microstructural analyses cover faults with dimensions spanning over five orders of magnitude, from microfaults of sub-millimeter length, to meter long faults (GF1 and GF2), and hundred meter long GF3. Fig. 16 presents the widths of the zones of the observed deformation structures across the analyzed set of faults. The widths of the zones are apparently proportional to the length L of the associated fault. The nature of the deformation is described below in terms of the zonation defined in Fig. 1.

4.1. Fault-core

The fault-core is the zone that accommodates the displacement between the two blocks of the fault (Chester et al., 1993). We identified the fault-core in the field as a dark, featureless band (GF1), or as a (micro) breccia-zone (GF2 and GF3). The displaced fractures of the E–W set could not be recognized inside the fault core due to obliteration by the localized shear. The simple shear strain

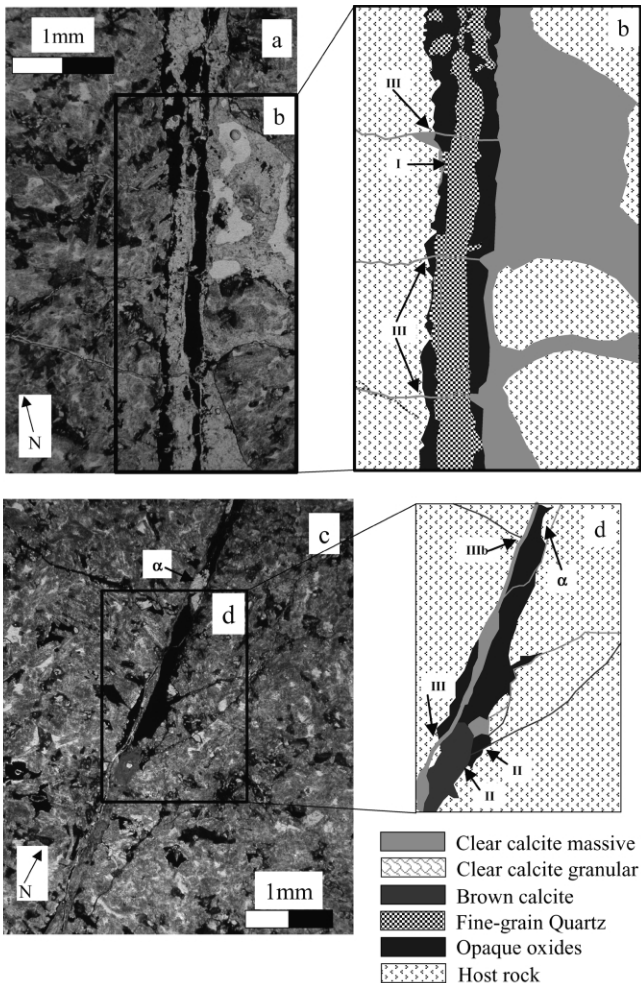

Fig. 11. Photomicrographs and maps of samples 108 ((a) and (b)) and 121 ((c)–(d)) at GF1 (locations shown in Fig. 4), showing the crosscutting relations of the fracture fillings. Opaque oxides are crosscut by fine-grain quartz (I at b), brown calcite (II at d) and clear calcite (III at b and d); fine-grain quartz is crosscut by clear calcite (III at b); brown (and greenish brown) calcite are crosscut by clear calcite (IIIb at d); Few rock fragments appear along the core (α at c, d).

in the fault-core is:

$$\gamma = S/2W_C$$

where S is fault slip and W_C is half the fault-core width as measured in the field. The shear strain is about 350% across GF1 core ($S \sim 35$ mm, $2W_C \sim 10$ mm), 200% across GF2 core ($S \sim 20$ mm, $2W_C \sim 10$ mm) and up to 500% across GF3 ($S = 125$ cm, $2W_C = 25$ cm; d–d″ area in Fig. 6). This localized shear leads to intense host rock deformation manifested by brecciaed rock fragments and closely spaced microfractures (Figs. 11 and 12). The visible fault-core width in the field is $\sim 0.001L$; the width is larger, 0.002–$0.004L$, for microfaults and small faults in triaxial tests (Fig. 16).

4.2. Damage-zone

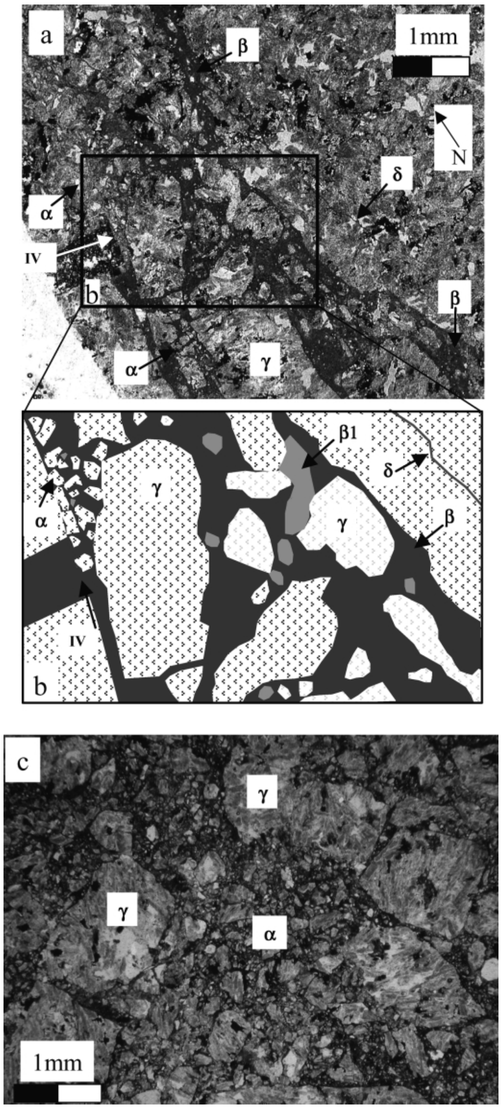

Fig. 12. Microstructure of GF2 (sample 117) and GF3 (sample 310), see Figs. 5, 6 and 15a for locations; legend in Fig. 11. (a) Photomicrograph and (b) map of GF2 core; it is brecciated with a few, partly linked bands in a generally north direction that contain angular rock fragments (marked α in (a) and (b)) in a matrix of brown, greenish-brown (β in (a) and (b)) or clear calcite (β_1 in (b)); large blocks of intact rock appear in the matrix between the zones (marked γ in (a) and (b)); a few E–W-striking fractures are cut and displaced by the breccia zones (IV in (a) and (b)); note a fault-parallel fracture in the upper-right (δ in (a) and (b)). (c) Photomicrograph of GF3 core which is a breccia zone with elongated bands of angular, poorly sorted rock fragments (center of the photomicrograph, marked α) cemented by brown calcite; large blocks of intact host rock occur between the zones (marked γ).

This is a wide zone of damaged rock in which the intensity of fault-related deformation gradually decreases outward (Chester et al., 1993). The damage-zone of the studied faults includes several deformation features. First, calcite-filled-networks (Fig. 11) and fault-parallel micro-fractures (Figs. 12 and 15) that occur in zones with fault normal widths of $0.005L$ and $0.02L$, respectively (Fig. 16). Second, competence reduction of the host rocks as revealed with the Schmidt hammer takes place over a zone up to $\sim 0.03L$ wide (Figs. 7 and 8). We suspect that the width of

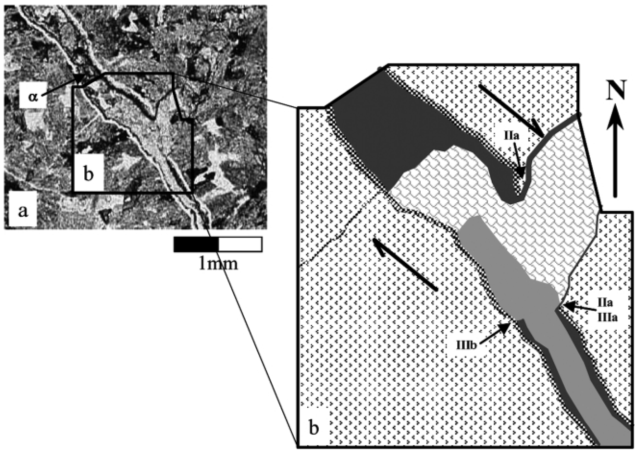

Fig. 13. (a) Photomicrograph and (b) map showing secondary minerals in a microfracture (sample 120, tip of GF2; for locations see Figs. 5 and 15; legend in Fig. 11). The minerals include clear calcite with massive and granular appearances; brown calcite in the fracture rims or center and fine-grain quartz; the brown calcite crosscuts the fine-grain quartz (IIa) and clear calcite crosscuts both of them (IIIa and IIIb, respectively); the brown calcite in the fracture center contains rock fragments (*α* in a) that lack in the clear calcite fill.

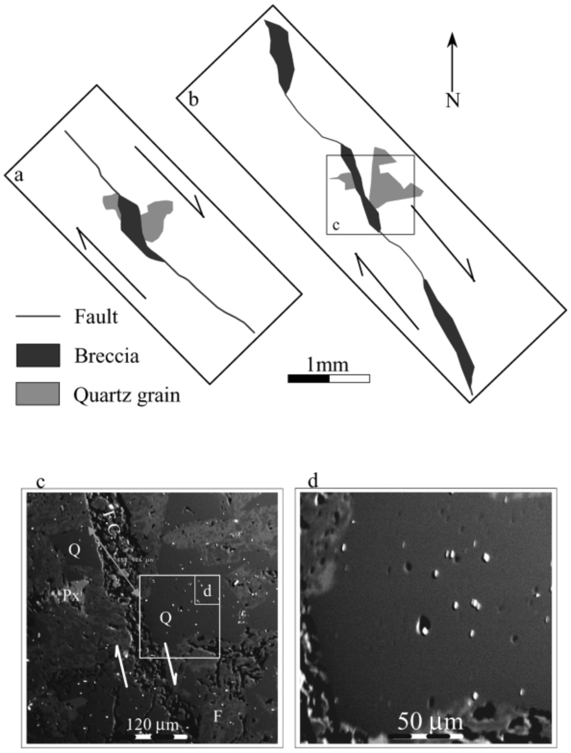

Fig. 14. Microfaults mapped on a thin section and SEM images (sample 115, location shown in Fig. 5). (a) and (b) Segmented, dextral microfaults with en-échelon geometry including micro pull-aparts filled with brown calcite and brecciated rock fragments; sheared quartz crystals reveal displacements of ~0.25 mm (locations are shown in Fig. 15). (c) SEM image of the microfault in (b); Q, F and Px are quartz, feldspar and pyroxene (aegirine) crystals and F.C. is fault core; note the extremely fine breccia inside F.C. (d) Close-up of a single quartz grain adjacent to the microfault in (c); note the lack of dilational microcracks.

the reduction zone near GF3 is an underestimation of the real width because the background Young modulus close to GF3 is lower by 6–7% than the equivalent close to the other two faults (Table 1). Third, distortion of fracture traces that vanish at a distance of 0.2–0.4 m away from GF2, and 4–6 m away from GF3 (Fig. 10); these distances are about 0.05–0.06 of the corresponding fault length (solid dots in Fig. 16).

4.3. Protolith

This is a region with negligible fault-related deformation, which extends outwards from the external limit of the damage-zone. The Schmidt hammer readings return to the background levels of the undeformed host rock.

5. Discussion

5.1. The process zone of brittle faulting

The concept of ‘process zone’ was introduced to incorporate the non-linear character of a fracture tip into linear elastic fracture mechanics framework (Lawn, 1993). Irwin (1958) divided the crack system into a linear-elastic outer zone that transmits the applied loading to the very small zone (process zone) around the fracture tip. The stresses in the process zone reflect the stress concentration and stress field at the fault tip (Lawn, 1993). Barenblatt (1962) and Dugdale (1960) described fracturing through a cohesive, plastic, process zone that is located in the propagating fracture tip in which energy absorption processes may operate. In brittle rocks, these energy absorption processes are primarily manifested by microcracking of the intact rock (Cowie and Scholz, 1992; Reches and Lockner, 1994). In the field, the dimensions of the process zone were determined by the occurrence of tensile microfractures (Anders and Wiltschko, 1994; Vermilye and Scholz, 1998) and large fractures (Little, 1995). It was shown in several field cases that the process zone width is about 0.01 the fault length (Cowie and Shipton, 1998; Vermilye and Scholz, 1998). Scholz et al. (1993) further used the Dugdale–Barenblatt concept and estimated that the process zone length scales with the process zone width. Another approach considers a constant value for the process zone width that is controlled by the stress intensity at the fault tip and by the mechanical properties of the host rock (Reches and Lockner, 1994; Lyakhovsky, 2001).

What is the nature of the process zone in Gevanim faults? Previous field studies used the abundant tensile microcracks to delimit the process zone (Anders and Wiltschko, 1994; Vermilye and Scholz, 1998). In our field area, however, the faults developed with negligible amounts of tensile microcracks (see above), and a different criterion is needed to define the process zone dimensions. We examine the two zones described above, the fault-core and the damage-zone

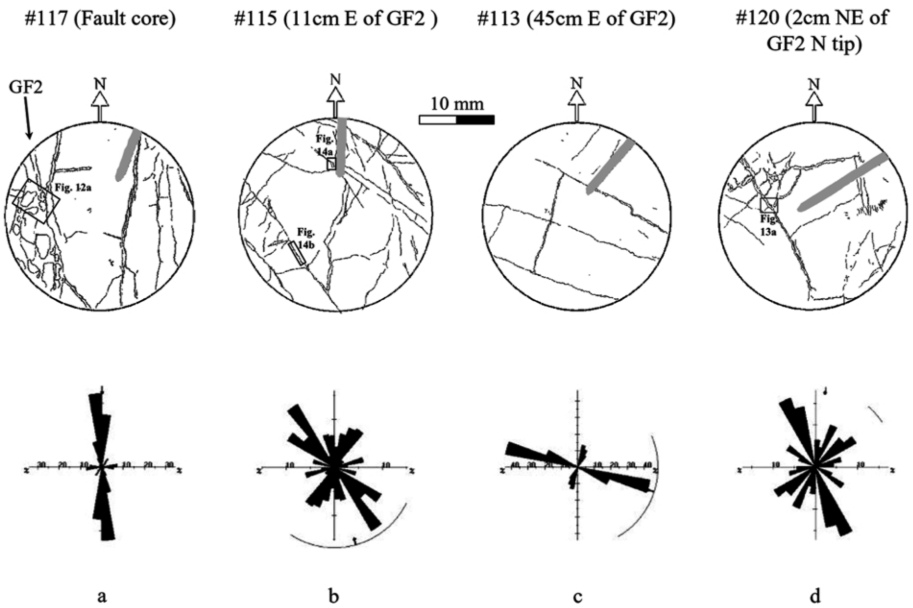

Fig. 15. Microstructural maps of GF2 samples (upper row) and corresponding fracture rose diagrams below (length-azimuth, area weighted); mapping at 40:1 scale of scanned images and an optical microscope; (a)–(c) samples 117, 115 and 113 across the fault (distances are marked), and (d) sample 120 NE from the northern tip area (locations of samples are shown in Fig. 5b). The areas mapped in detail and shown in Figs. 12a, 13a and 14a and b are marked. In gray are unmapable notches on the sections surface used to orientation inference.

(see Section 4). The fault-core contains breccia (Figs. 11–13) and underwent large simple shear (200–500%), and it is a region of breakdown and disintegration of the intact host rock. Thus, the fault-core is likely to be considered as part of the process zone; a portion of the simple shear could reflect the slip that post-dated the fault formation. The situation is different with the damage-zone. It contains fault-parallel shear microfractures and calcite-filled networks but it retains its physical coherence. Thus, it is unlikely that the damage-zone is part of the process zone.

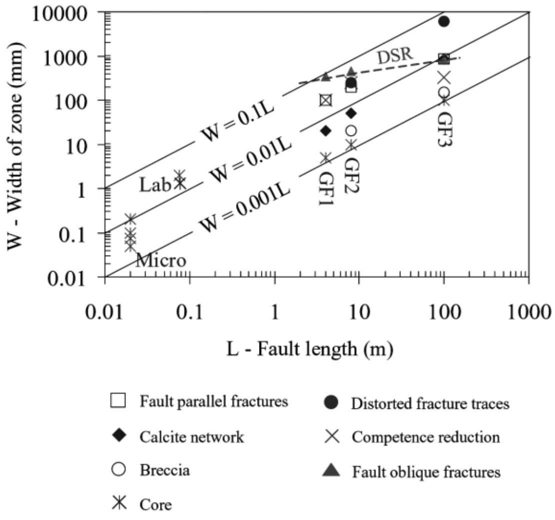

Fig. 16. Zonation of host rock deformation across faults in Gevanim quartz–syenite. Shown maximum fault normal width (*W*, defined in Fig. 9) of the marked structural features versus length of the associated faults (*L*) (see text and Table 2). Micro—indicates observations along microfaults in thin-sections (Figs. 14 and 15); Lab—indicates faults in Gevanim quartz–syenite that developed in triaxial failure tests (Katz, 2002); field data is marked with host fault name (GF1, GF2, GF3); DSR—a dashed line indicating the range limit of the field survey for fault related deformation; note that the width of the calcite-network and the fault-parallel microfractures across GF3 is bounded by the sampling distance.

The present interpretation restricts the use of the ‘process zone’ to the region of breakdown, disintegration and extreme strain, which in the present study corresponds to the fault-core. The process zone width according to this interpretation is smaller than the one recognized in previous works; it is 0.001–0.005*L* in the present work (Fig. 16) whereas it is about 0.01*L* in Anders and Wiltschko (1994) and Vermilye and Scholz (1998).

5.2. Evolution of host rock deformation along Gevanim faults

In this section we discuss the evolution of the fault-related deformation of the studied faults by outlining the pre-faulting stage and faulting stage; the post-faulting deformation is analyzed in Part II. It is anticipated that pre-faulting deformation will display a quasi-uniform distribution (Reches and Lockner, 1994; Lyakhovsky et al., 1997). Our observations, however, of rock brecciation (Fig. 12), reduction of rock competence (Fig. 8), and the distribution of shear and tensile microfractures (Fig. 15) are all restricted to a zone narrower than ~0.03 the fault length (Fig. 16). The restriction of these features to the faults proximity indicates that they are not pre-faulting structures. Further, it is also commonly accepted that tensile microfractures dominate the pre-failure damage of brittle rocks (Peng and Johnson, 1972; Hadley, 1976; Horii and Nemat-Nasser, 1985; Reches and Lockner, 1994). The outstanding lack of tensile microfractures in Gevanim quartz–syenite (see Section 3) indicates that the studied faults formed by a mechanism that is not based on tensile microfracturing.

We suggest that the faults in the quartz–syenite grew as primary shear fractures based on observations of shear fractures over wide range of sizes (Figs. 4–6 and 11–13). These fractures revealed striking geometric similarities regardless of scale: (1) the shear fractures are composed of linked segments (Figs. 4–6, 14 and 15); (2) the segments are slightly crooked to quasi-linear (Figs. 4–6 and 14); and (3) tensile microfractures that are related to the faults are practically missing down to scale of 5 μm (Fig. 14d). This self-similarity suggests that the faults grew by the same mechanism from the intergranular micro-shears (Fig. 14) to the 100-m-long fault (Fig. 3). We envision that this growth occurred first by lengthening of the intragranular micro-shears in their own plane, followed by their coalescence with other micro-shears to form the segmented micro-fault (Reches, 1987, 1988) (Fig. 14). This sequential process of lengthening and coalescence continued and eventually forms faults of a meter length and more. Finally, the observed self-similarity suggests that the three mapped faults represent different stages of fault development. Faults GF1 and GF2 are relatively ‘young’ with minor amounts of breccia and thin fault-core, whereas GF3 is already in a ‘mature’ stage.

During the faulting stage, the propagating faults generated highly localized deformation in the process zone manifested primarily as micro-breccia and high shear in the fault-core (Fig. 12). The scarcity of gouge material (Figs. 11 and 12) indicates that continuous wear along the faults was probably negligible.

The distorted fracture traces presented above (Fig. 15) is interpreted by us as indicating continuous post-faulting deformation of the host rock. The analysis and justification for this conclusion are presented in Part II.

6. Concluding remarks

The structural analysis of the quartz–syenite body in Gevanim reveals the following characteristics of the faults and their associated deformation.

Fault dimensions. The dimensions of the studied fractures span over five orders of magnitude (Fig. 16). The spacing of the faults is not uniform. The fault parallel microfaults, 1–10 mm long, are restricted to zones along the longer faults (Figs. 15 and 16). The spacing of the medium-size faults, 1–10 m in length, is at approximately the fault length, 1–5 m (Fig. 3). The 100-m-long fault is unique within the $\sim 0.3\ \mathrm{km}^2$ study area (Figs. 2a and 3). A noticeable negative observation is the scarcity of tensile microcracks in the analyzed rocks.

Geometry of fault traces. The mapped faults display fairly continuous traces that are curved and irregular from the <1 mm scale (Fig. 14c), through the microfaults (Fig.14a and b) to the field scale faults of GF1, GF2 and GF3 (Figs. 4–6). Part of the irregular shape is a manifestation of the segmented nature of the faults, starting from 1–10-mm-long faults (Fig. 14) to a maximum recognized length of an individual segment of about 1 m (GF1 and GF2 in Figs. 4 and 5).

Fault-related deformation. Deformation indicators include fault displacement, breccia zones, fault-related microstructures, distortion of fracture traces and competence reduction. Each of these indicators is distributed along the associated faults within a zone of characteristic width (Fig. 16).

Timing of fault-related deformation. Fault-related deformation was formed during two main episodes: (1) during fault propagation when highly localized deformation occurred within the process zone. This deformation is restricted to the fault core with width of 0.001–0.005 of fault length; (2) post-faulting deformation of the host rock that is analyzed in Part II. One noticeable result is that none of the deformation indicators could be clearly attributed to the pre-faulting stage of distributed damage.

Fault growth mechanism. We observed self-similarity of the discontinuities over five length orders-of-magnitude and an outstanding lack of tensile microcracks. These observations suggest that fault growth occurred in shear, mode II/III, without contribution of tensile fracturing (Katz and Reches, 2000). Evidence and implications of this mechanism are the subject of future research (Katz et al., in preparation).

Acknowledgements

The fieldwork accomplished with the invaluable technical support of Ya’akov Refael and Shlomo Ashkenazi from the Geological Survey of Israel. Discussions with Vladimir Lyakhovsky significantly contributed to the quality of this study. The critical reviews of Jan M. Vermilye and an anonymous reviewer significantly improved the manuscript and their comments are greatly appreciated. Thanks to Rod Holcombe for the permit to use the GeOrient program. The study was partially supported by the US–Israel Binational Scientific Foundation grant 98-135, and by the Geological Survey of Israel project 30255.

References

Anders, M.H., Wiltschko, D.V., 1994. Microfracturing, paleostress and the growth of faults. Journal of Structural Geology 16, 795–815.

Ashby, M.F., Sammis, C.G., 1990. The damage mechanics of brittle solids in compression. Pure and Applied Geophysics 133, 489–521.

Aydin, A., Johnson, A.M., 1978. Development of faults as zones of deformation bands and as slip surfaces in sandstone. Pure and Applied Geophysics 116, 931–942.

Baer, G., Reches, Z., 1989. Doming mechanisms and structural development of two domes in Ramon, Southern Israel. Tectonophysics 166, 293–315.

Barenblatt, G.I., 1962. The mathematical theory of equilibrium cracks in brittle fracture. Advances in Applied Mechanics 7, 55.

Caine, J.S., Evans, J.P., Forster, C.B., 1996. Fault zone architecture and permability structure. Geology 24, 1025–1028.

Chester, F.M., Logan, J.M., 1986. Implications for mechanical properties of brittle faults from observations of the Punchbowl fault zone, California. Pure and Applied Geophysics 124, 79–106.

Chester, F.M., Evans, J.P., Biegel, R.L., 1993. Internal structure and weakening mechanisms of San Andreas Fault. Journal of Geophysical Research 98, 771–786.

Chinnery, M.A., 1966. Secondary faulting; Part 1. Theoretical aspects; Part 2. Geological aspects. Canadian Journal of Earth Sciences 3, 163–190.

Cowie, A.P., Shipton, Z.K., 1998. Fault tip displacement gradients and process zone dimensions. Journal of Structural Geology 20, 983–997.

Cowie, P.A., Scholz, C.H., 1992. Physical explanation for the displacement–length relationship of faults using a post-yield fracture mechanics model. Journal of Structural Geology 14, 1133–1148.

Dugdale, D.S., 1960. Yielding of steel sheets containing slits. Journal of Mechanics and Physics of Solids 8, 100.

Freund, R., 1974. Kinematics of transform and transcurrent faults. Tectonophysics 21, 93–134.

Griffith, A.A., 1924. The theory of rupture. In: Biezeno, C.B., Burgers, J.M. (Eds.), Proceeding of First International Congress of Applied Mechanics, J. Waltman Jr, Delft, p. 55.

Hadley, K., 1976. Comparison of calculated and observed crack densities and seismic velocities in Westerly Granite. Journal of Geophysical Research, 81, 3484–3494.

Horii, H., Nemat-Nasser, S., 1985. Compression-induced microcrack growth in brittle solids: axial splitting and shear failure. Journal of Geophysical Research 90, 3105–3125.

Irwin, G.R., 1958. Fracture. Handbuch der Physik, Springer-Verlag, Berlin 6.

Itamar, A., Baer, G., 1993. Polymetallic mineralization related to magmatic and contact metasomatic features, southern Makhtesh Ramon, Israel. Israel Journal of Earth Sciences 42, 149–163.

Itamar, A., Steinitz, G., 1988. Potassium argon ages of polymetallic mineralization in the Gavnunim valley, Makhtesh Ramon Israel. Israel Journal of Earth Sciences 37, 83–89.

Katz, O., 2002. Mechanisms of fault nucleation in brittle rocks. Ph.D. dissertation, Hebrew University, Jerusalem.

Katz, O., Reches, Z., 2000. Micro and macro structural analysis of small faults in a qz–syenite intrusion: faulting of a brittle rock without microcracking? American Geophysical Union, Fall Meeting, San Francisco.

Katz, O., Reches, Z., Roegiers, J.-C., 2000. Evaluation of mechanical rock properties using a Schmidt hammer. International Journal of Rock Mechanics and Mining Sciences 37, 723–728.

Krantz, L.K., 1979. Crack growth and development during creep in Westerly granite. International Journal of Rock Mechanics and Mining Sciences 16, 23–36.

Lang, B., Steinitz, G., 1989. K–Ar dating of mesozoic magmatic rocks in Israel: A review. Israel Journal of Earth Sciences 38, 89–103.

Lawn, B., 1993. Fracture of Brittle Solids, 2nd ed, Cambridge Solid State Science Series, Cambridge University Press.

Little, T.A., 1995. Brittle deformation adjacent to the Awatere strike slip fault in New Zealand; faulting patterns, scaling relationships and displacement partitioning. Geological Society of America Bulletin 107, 1255–1271.

Lyakhovsky, V., 2001. Scaling of fracture length and distributed damage. Geophysical Journal International 144, 114–122.

Lyakhovsky, V., Ben-Zion, Y., Agnon, A., 1997. Distributed damage, faulting and friction. Journal of Geophysical Research 102, 27635–27649.

Moore, D.E., Lockner, D.A., 1995. The role of microcracking in shear-fracture propagation in granite. Journal of Structural Geology 17, 95–114.

Peng, S., Johnson, A.M., 1972. Crack growth and faulting in cylindrical specimens of Chelmsford granite. International Journal of Rock Mechanics and Mining Sciences 9, 37–86.

Pollard, D.D., Segall, P., 1987. Theoretical displacements and stresses near fractures in rock; with applications to faults, joints, veins, dikes, and solution surfaces. In: Atkinson, B.K., (Ed.), Fracture Mechanics of Rock, Academic Press, London, pp. 277–349.

Reches, Z., 1987. Mechanical aspects of pull-apart basins and push-up swells with applications to the Dead Sea transform. Tectonophysics 141, 75–88.

Reches, Z., 1988. Evolution of fault pattern in clay experiments. Tectonophysics 145, 141–156.

Reches, Z., Lockner, D.A., 1994. The nucleation and growth of faults in brittle rocks. Journal of Geophysical Research 99, 18,159–18,174.

Scholz, C.H., Dawers, N.H., Yu, J.Z., Andres, M.H., Cowie, P.C., 1993. Fault growth and scaling laws: preliminary results. Journal of Geophysical Research 98, 21,951–21,961.

Segall, P., Pollard, D.D., 1980. Mechanics of discontinuous faults. Journal of Geophysical Research 85, 4337–4350.

Suppe, J., 1985. Principles of Structural Geology, Prentice-Hall, New Jersey, 537pp.

Sylvester, A.G., 1988. Strike slip faults. Geological Society of America Bulletin 100, 1666–1703.

Tapponnier, P., Brace, W.F., 1976. Development of stress-induced microcracks in westerly granite. International Journal of Rock Mechanics and Mining Sciences and Geomechanical Abstracts 13, 103–112.

Vermilye, J.M., Scholz, C.H., 1998. The process zone; a microstructural view of fault growth. Journal of Geophysical Research 103, 12,223–12, 237.

Zak, Y., 1960. The Geological Map of Israel, Makhtesh Ramon-Har Gevanim Sheet. Geological Survey of Israel.